PHOTONICS Research

Ultrahigh detectivity, high-speed and low-dark current AlGaN solar-blind heterojunction field-effect phototransistors realized using dual-float-photogating effect

Kai Wang,[1,†] Xinjia Qiu,[1,†] Zesheng Lv,[1] Zhiyuan Song,[1] and Hao Jiang[1,2,3,*]

[1]School of Electronics and Information Technology, Sun Yat-sen University, Guangzhou 510275, China
[2]State Key Laboratory of Optoelectronic Materials and Technologies, Sun Yat-sen University, Guangzhou 510275, China
[3]Guangdong Engineering Technology R & D Center of Compound Semiconductors and Devices, Sun Yat-sen University, Guangzhou 510275, China
*Corresponding author: stsjiang@mail.sysu.edu.cn

Received 28 September 2021; revised 31 October 2021; accepted 4 November 2021; posted 4 November 2021 (Doc. ID 444444); published 13 December 2021

High detectivity is essential for solar-blind deep-ultraviolet (DUV) light detection because the DUV signal is extremely weak in most applications. In this work, we report ultrahigh-detectivity AlGaN-based solar-blind heterojunction-field-effect phototransistors fabricated utilizing dual-float-photogating effect. The p^+-$Al_{0.4}GaN$ layer and $Al_{0.4}GaN$ absorber layer deposited on the $Al_{0.6}GaN$ barrier serve as top pin-junction photogate, while the thin $Al_{0.4}GaN$ channel layer with a strong polarization field inside acts as virtual back photogate. Due to the effective depletion of the two-dimensional electron gas at the $Al_{0.6}Ga_{0.4}N/Al_{0.4}Ga_{0.6}N$ heterointerface by the top photogate, the dark current was suppressed below 2 pA in the bias range of 0 to 10 V. A high photo-to-dark current ratio over 10^8 and an optical gain of 7.5×10^4 were demonstrated at a bias of 5 V. Theoretical analysis indicates that the optical gain can be attributed to the joint action of the floating top and back photogates on the channel current. As a result, a record high flicker noise (Johnson and shot noise) limited specific detectivity of 2.84×10^{15} (2.91×10^{17}) cm $Hz^{0.5}$ W^{-1} was obtained. Furthermore, high response speed at the microsecond level was also shown in the devices. This work provides a promising and feasible approach for high-sensitivity DUV detection. © 2021 Chinese Laser Press

https://doi.org/10.1364/PRJ.444444

1. INTRODUCTION

Recent progress in preparing ultrawide-bandgap semiconductors has greatly promoted the research of solid-state ultraviolet detection, especially the solar-blind photodetection inside the deep-ultraviolet (DUV) band (wavelength of 200 to 280 nm). Regardless of solar background light, solar-blind photodetectors have significant applications in the fields such as corona discharge and flame detection, fire warning, short-range communication, and biological imaging [1–3]. In most applications, however, the received solar-blind DUV signal is extremely weak due to the very small amount of DUV radiation from the signal source and the high attenuation of DUV transmission in the atmosphere. Therefore, the detectivity, a figure of merit of photodetectors describing the minimum detectable optical signal, needs to be high in the practical solar blind detection. The key to achieving a high detectivity is to improve the responsivity through optical gain while keeping the dark current low.

AlGaN is one of the most promising materials for solar-blind DUV detection because of its tunable direct bandgap corresponding to the DUV spectral region and its advances in epitaxial growth and processing technologies. AlGaN-based heterojunctions with high-density two-dimensional electron gas (2DEG) at the heterojunction interface have been successfully used not only in high electron mobility transistors [4] but also for high-responsivity UV photodetectors [5,6]. Benefiting from the high conductivity of 2DEG channel, AlGaN-based UV heterojunction field effect phototransistors (HFEPTs) can generally exhibit an ultrahigh photoconductive gain and the resulting high responsivity. Although the photoconductive gain of AlGaN HFEPT can match or even exceed the optical gain of the typical gain-type photodetectors, such as avalanche photodiodes [7,8] and heterojunction phototransistors [9,10], the conductivity of 2DEG channel also leads to high dark current, which reduces the detectivity [11,12].

One solution is to deposit a p^+-type layer on the barrier layer to form a floating p-n-junction photogate, so as to effectively deplete the 2DEG under the gate and suppress the dark current, but also open the 2DEG channel driven by the photovoltage generated by the UV incident light [13,14]. Compared with the scheme of adding a negatively-biased metal gate [15,16], the floating p-type photogate can be used to construct two-terminal HFEPTs, which have the advantages of low power consumption and on-chip integration. However, for AlGaN-based solar-blind HFEPTs, the achievement of p-type photogate is hindered by the very low doping efficiency in high Al-content $Al_xGa_{1-x}N$ ($x > 0.4$) due to the high activation energy of the Mg acceptor, the low solubility of the acceptor dopant, and the strong self-compensation effect. For this reason, so far, there is no report on AlGaN solar-blind UV HFEPT with p-type photogate.

In addition to the barrier side of the AlGaN heterojunction, the conductivity modulation of 2DEG channel by the photovoltage may also be achieved from the channel layer side. It is expected to further improve the performance characteristics of AlGaN solar-blind HFEPT by introducing the photovoltage effect into the channel layer via manipulating the strain-induced polarization field.

In this work, $Al_{0.6}GaN/Al_{0.4}GaN$ solar-blind DUV HFEPTs with interdigitated electrode geometry were fabricated by utilizing dual-float-photogating effect. A p^+-$Al_{0.4}Ga_{0.6}N$ layer and an $Al_{0.4}GaN$ absorption layer were grown on the $Al_{0.6}GaN$ barrier to form a top floating photogate. High hole concentration was obtained in the p-type layer by using Mg doping-interface effects to deplete the 2DEG under the photogate and pinch off the conduction path. A thin $Al_{0.4}GaN$ channel layer was designed on AlN/sapphire template to ensure the energy band tilt of the whole channel layer due to the compression strain induced polarization field, so as to enhance the back-photogate effect regulated by the photocarriers generated by the channel layer absorption of incident light. The fabricated devices exhibit very low dark current and high photo-dark current ratio. Ultrahigh optical gain was obtained due to the dual-float-photogating effect. As a result, a record high flicker noise (Johnson and shot noise) limited specific detectivity of 2.84×10^{15} (2.91×10^{17}) cm $Hz^{0.5}$ W^{-1} was achieved. These excellent performances make the proposed photodetector a very promising candidate for solar-blind DUV detection.

2. EXPERIMENTAL SECTION

Samples used in this work were grown on *c*-plane sapphire substrates by metal-organic chemical vapor deposition (MOCVD) in a low-pressure reactor. The epilayers, from bottom to top, consist of a 500 nm thick AlN buffer layer deposited at 1080°C, a 160 nm thick unintentionally doped (uid) $Al_{0.4}Ga_{0.6}N$ as a channel layer, a 25 nm thick uid-$Al_{0.6}Ga_{0.4}N$ barrier layer, a 50 nm thick uid-$Al_{0.4}Ga_{0.6}N$ as an absorber layer, and a 60 nm thick Mg-doped p-type $Al_{0.4}Ga_{0.6}N$ gate layer grown by utilizing doping interface effects [17]. Using the Hall-effect measurements, the hole concentration in the p-$Al_{0.4}GaN$ gate layer is determined to be $\sim 8 \times 10^{18}$ cm^{-3}, which is to exhaust the 2DEG generated at the interface between the barrier layer and the channel layer and thus decrease the dark current of the devices. For comparison, a control structure (HFEPT) was also prepared with the same growth parameters and epitaxial structure except for the p^+-$Al_{0.4}GaN$ gate and the absorber layer. This wafer sample shows a 2DEG mobility of 130 cm^2 V^{-1} s^{-1} and a sheet density of $7.5 \times 10^{12}/cm^2$. The relatively low mobility is attributed to the large electron effective mass in $Al_{0.4}GaN$ and the alloy scattering at the $Al_{0.6}GaN/Al_{0.4}GaN$ heterointerface.

Device fabrication was started with p^+-$Al_{0.4}GaN$ patterning, using inductively coupled plasma (ICP) dry etching down to the uid-$Al_{0.6}GaN$ barrier layer, to form p-AlGaN stripes as the top photogate. Then the Ohmic-contact electrodes were formed on the exposed uid-$Al_{0.6}Ga_{0.4}N$ barrier using Ti (15 nm)/Al (80 nm)/Ni (20 nm)/Au (60 nm) metal stacks annealed at 830°C for 30 s in N_2 ambient. The Ohmic-contact electrodes were patterned by a lift-off process to form the interdigitated electrodes to increase the carrier collection rate of the electrodes and increase the illumination receiving area. The fingers of the interdigitated electrodes were 45 μm wide with a spacing of 12 μm and the active area was 50 μm × 183 μm for the photodetectors. A schematic diagram of the HFEPT structure (named PG-HFEPT) utilizing dual-float-photogating effect is shown in Fig. 1.

Transmittance and reflection spectra of the deposited epilayers grown on double-side polished (0001) sapphire substrates were recorded using a Shimadzu UV2550 ultraviolet-visible spectrophotometer. X-ray diffraction (XRD) reciprocal space mapping (RSM) was applied to characterize the epitaxial structure. The RSM measurements were carried out using a high-resolution XRD instrument (Bruker D8 DISCOVERY). Current-voltage (I-V) characteristics of the fabricated devices were analyzed using a Keithley 4200-SCS semiconductor parameter analyzer under dark and DUV-illuminated conditions. The fabricated photodetectors were illuminated from the top side and the incident light source was a deep-UV light-emitting diode with a peak wavelength of 260 nm. Spectral responses were measured in the 200 to 400 nm wavelength

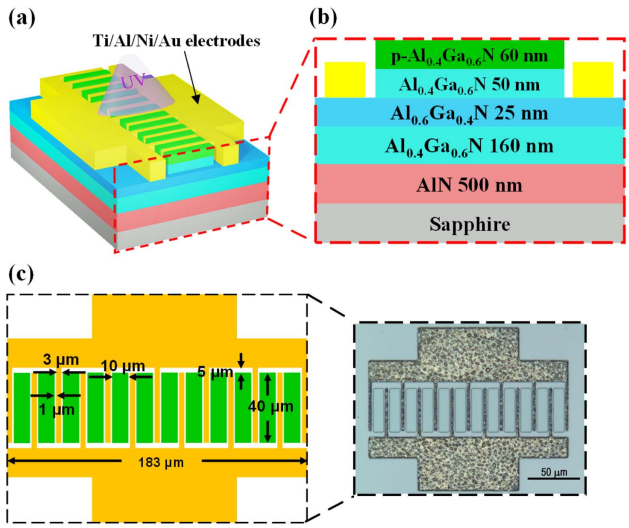

Fig. 1. (a) Schematic illustration of the PG-HFEPT and (b) its cross-sectional view. (c) Schematic diagram and optical image of the interdigitated electrodes, mentioning the device dimensions.

range under the different bias voltages at room temperature using a xenon/deuterium lamp and a monochromator with 1200 g/mm grating as the light source. A Newport power meter was used to determine the incident power densities over the measuring range. Time-dependent photoresponse was measured by modulating the output light from the monochromator using an electronic shutter with a timing resolution of 1 ms. In the measurement, the modulation period of the light source is 60 s, including 30 s on time and 30 s off time. The transient response of the fabricated devices was investigated using a high-speed oscilloscope (6 GHz, Keysight DSOS604A) excited by a 260 nm UV laser with pulse width of 625 ps and repetition frequency of 1 kHz. Noise spectra were collected by an FS-Pro multifunctional semiconductor parameter tester.

3. RESULTS AND DISCUSSION

The optical and structural properties of the epitaxial sample were at first characterized. It can be seen from the transmission spectrum that the absorption edge of $Al_{0.4}GaN$ layers is at 277 nm. Similarly, the relative reflectance spectrum of the heterostructure also indicates that the $Al_{0.4}GaN$ reflection peak is located at this wavelength [Fig. 2(a)] [18]. Besides, the transmittance is less than 34.4% at 277 nm, indicating that the incident DUV signal from the top side can generate electron–hole pairs (EHPs) not only in the uid-$Al_{0.4}GaN$ absorber layer but also in the whole uid-$Al_{0.4}GaN$ channel layer. Figure 2(b) gives the XRD-RSM pattern of the epitaxial structure with p^+-$Al_{0.4}GaN$ taken around the asymmetric (105) reflection. The Al compositions are estimated to be 59% and 42% for the barrier and channel layers. It can also be found that the $Al_{0.4}GaN$ channel layer is largely strained to the AlN template layer as shown by the relaxation degree of 39.1%. The relaxation degree ($R\%$) in the $Al_{0.4}GaN/AlN$ heterostructure was determined from $R\% = 1 - \varepsilon_{meas}/\varepsilon_{coh}$, where ε_{coh} is the elastic strain in the fully coherent $Al_{0.4}GaN$ channel layer in assumption of the full relaxation of the AlN template layer and ε_{meas} is the elastic strain value measured from RSM [19]. In principle, the less the in-plane compression strain of relaxation, the stronger the piezoelectric polarization field in the channel layer [20], which has a positive impact on the separation of photogenerated electron–hole pairs in the channel layer and the resulting photovoltage regulation.

Considering the effects of spontaneous and piezoelectric polarization, the energy band diagrams of the epitaxial samples with and without p^+-$Al_{0.4}GaN$ photogate were numerically simulated using a 2D self-consistent Poisson–Schrödinger solver. As can be seen from Fig. 2(c), the conduction band level (E_C) at the barrier/channel interface is lower than the Fermi energy level (E_f) in the structure without the p^+- photogate, forming 2DEG the heterointerface. In contrast, as shown in Fig. 2(d), in the structure with a p^+-$Al_{0.4}GaN$ photogate, the E_C at the heterointerface is elevated to 45.3 meV higher than the E_f, indicating that there is no 2DEG accumulated at the heterointerface. The simulation results, therefore, show that the layer thickness and carrier concentration in the p^+-i-n structure, including the absorption and barrier layers, can just satisfy the requirement for 2DEG depletion. On the other hand, due to the strain-induced polarization field, the energy band of the whole layer of the 160 nm thick uid-$Al_{0.4}GaN$ channel layer on the AlN buffer is inclined. The resulting large potential difference in the channel layer can be regulated by the incident photogenerated carriers, thus acting as a back photogate.

Figures 3(a) and 3(b) compare the *I-V* characteristics of the two-terminal PG-HFEPT and HFEPT measured in dark and DUV illuminated conditions. For the PG-HFEPT, the dark current (I_{dark}) is less than 2.0×10^{-12} A in the range of 0 to 10 V and as low as 7.8×10^{-13} A at 5 V bias, benefiting from the effective depletion of 2DEG by the p^+-$Al_{0.4}GaN$ photogate. Under the DUV illumination with a central

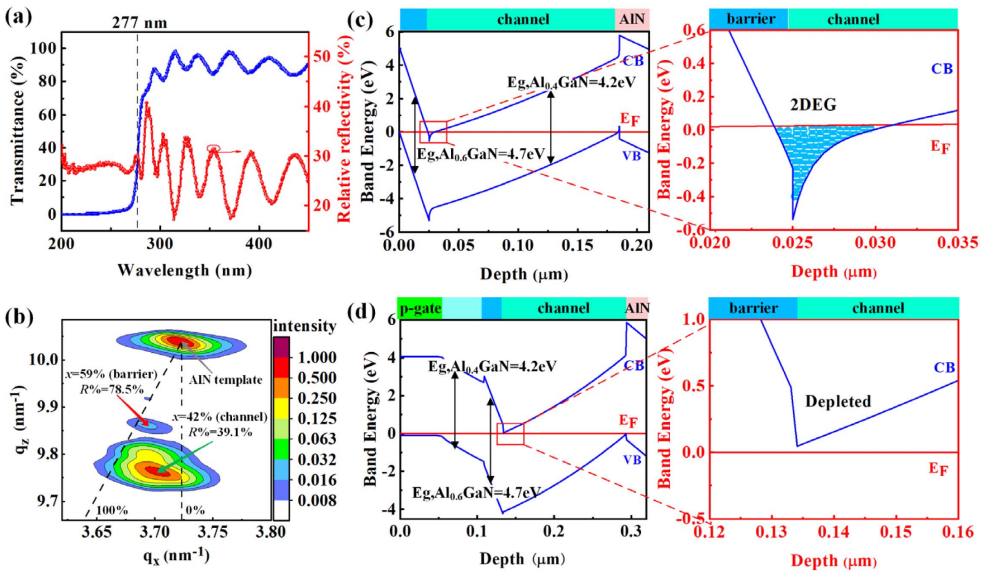

Fig. 2. (a) Transmission and reflection spectra of the epitaxial structure with p-type photogate. (b) XRD RSM for the epitaxial structure taken around (105) reflection, in which the dashed lines correspond to fully strained ($R\% = 0\%$) and fully relaxed ($R\% = 100\%$) states of the $Al_{0.4}GaN$ channel layer. Simulated energy band diagram for the devices (c) without and (d) with the p-type AlGaN photogate.

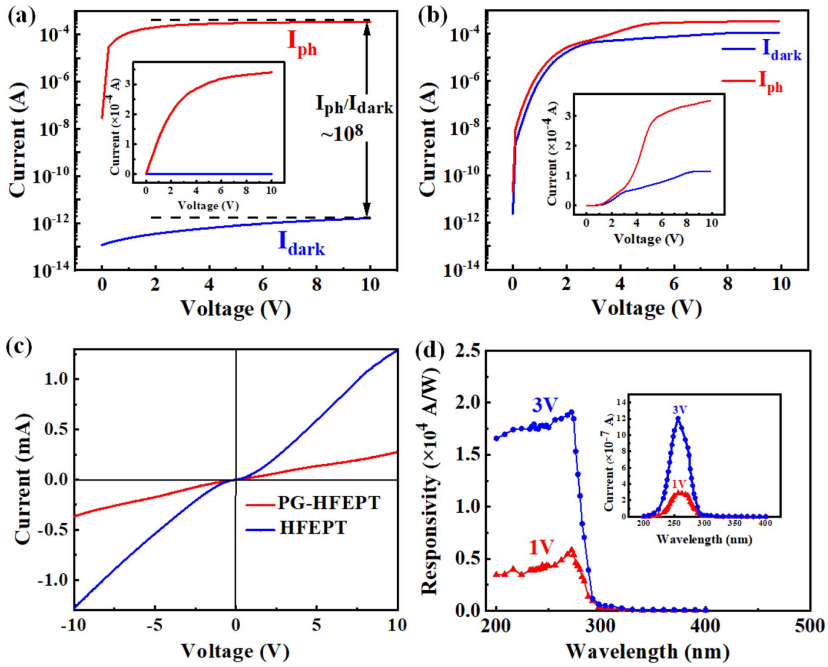

Fig. 3. Dark and illuminated *I-V* characteristics of the HFEPTs (a) with and (b) without the p^+-$Al_{0.4}GaN$ top photogate. The inset of (b) is the linear plot of the *I-V* curve. (c) *I-V* characteristics of the Ti/Al/Ni/Au Ohmic electrodes for the two HFEPTs. (d) Spectral responsivity of the PG-HFEPT under 1 V and 3 V bias. The inset is the corresponding spectral photocurrent.

wavelength of 260 nm and an intensity of 220 μW/cm^2, a high photocurrent (I_{ph}) of 3.1×10^{-4} A was obtained at 5 V bias as shown in Fig. 3(a). Consequently, an ultrahigh photo-to-dark current ratio of more than 10^8 is obtained over the entire bias range except for the near-zero bias. For the HFEPT, however, the I_{dark} is 6.8×10^{-5} A and the I_{ph} is 2.7×10^{-4} A at 5 V bias [Fig. 3(b)]. In the absence of the p^+-$Al_{0.4}GaN$ photogate, the highly conductive 2DEG channel leads to a remarkable increase in the I_{dark}, while the I_{ph} is comparable to that of PG-HFEPT. Under the bias voltage of 10 V, the I_{ph} of both devices reaches about the same value (~3.5×10^{-4} A). The Ohmic-contact characteristics in Fig. 3(c), however, show that the contact resistance of PG-HFEPT is significantly greater than that of HFEPT, which is due likely to the surface defects induced by ICP etching during the removal of the p^+-layer. Higher I_{ph} is thus expected for the PG-HFEPT by decreasing the Ohmic contact resistance and consequently improving the transconductance. The above results indicate that the p^+-photogate effectively reduces the I_{dark} by depleting the 2DEG channel underneath, while the photogenerated carriers in the absorption layer may counteract the depletion, so that the photocurrent does not decrease.

The optical gain can be estimated from $G = (I_{ph} - I_{dark})h\nu/\eta_{ext}qP_{in}$, where $\Delta I_{ph} = I_{ph} - I_{dark}$ is the net channel photocurrent, $h\nu$ is the incident photon energy, η_{ext} is external quantum efficiency, q is the electronic charge, and P_{in} is the incident optical power. Assuming that the η_{ext} is 100%, the optical gains of PG-HFEPT and HFEPT are conservatively calculated to be 7.5×10^4 and 4.9×10^4 at 5 V bias, respectively. The spectral responsivity of the PG-HFEPT was also measured [Fig. 3(d)]. It can be observed that the cutoff wavelength of the HFEPTs was ~280 nm, due to the absorption edge of $Al_{0.4}GaN$ layers. At the bias voltage of 1 V, a peak responsivity of 5.8×10^3 A/W was obtained at 272 nm. As the bias voltage increases from 1 to 3 V, the peak responsivity increases to 1.9×10^4 A/W. Moreover, a spectral rejection ratio of ~1.6×10^2 between 280 and 400 nm was observed at a weak light intensity of 0.4 μW/cm^2 and a bias voltage of 3 V.

To illustrate the high gain mechanism of the PG-HFEPT, we analyze the factors contributing to the I_{ph} in the device. For DUV photons incident from the top side, there are three main regions that can absorb the photons and generate EHPs, namely, the absorber layer, barrier layer, and channel layer as shown in Fig. 4(a). When the EHPs are photogenerated in the absorber layer and the barrier layer underneath the p-type gate, the photoelectrons are swept to the heterojunction interface contributing to the channel 2DEG, while the photoholes are driven toward the p-type gate and accumulated there due to the vertical built-in field in the depletion region of the gate. This accumulation of photoholes leads to a lowering in the energy bands shown in Fig. 4(b), equivalent to a positive bias applied to the p-i-n heterojunction of the gate (i.e., photovoltage). As a result, the depletion region of the p-type gate shrinks, and the 2DEG channel turns on.

In the channel layer region, the photogenerated electrons also drift into the 2DEG channel by the built-in field (downward bending of the band) pointing to the substrate. In contrast, the photogenerated holes move toward the uid-$Al_{0.4}GaN$/AlN interface. Since there is no neutral region in the uid-$Al_{0.4}GaN$ channel layer and the AlN buffer layer is highly insulated, the holes accumulate near the interface due to the low recombination probability. The accumulation of

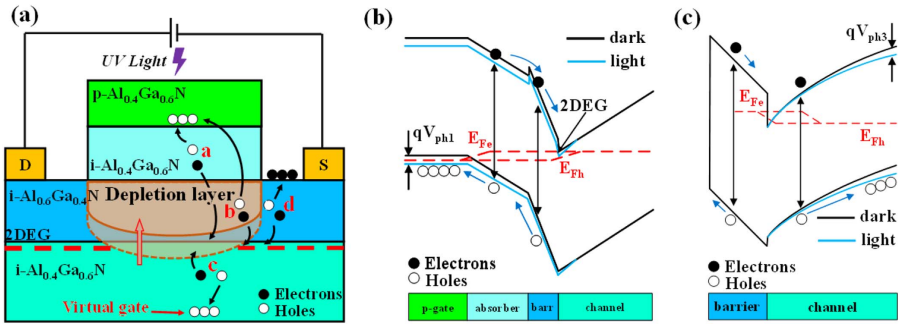

Fig. 4. (a) Schematic diagram of the photogenerated carriers and their movement in the absorber, barrier, and channel layers of PG-HFEPT. Schematic band diagrams of (b) the top p-type photogate heterojunction and (c) the virtual back-photogate heterojunction together with the barrier layer outside the p-photogate under dark and illumination conditions.

holes shifts the bands as shown in Fig. 4(c) and acts as a positive back-gate bias. That is, a photovoltage is created in this region due to the generation and separation of EHPs under the DUV illumination.

In addition, for the barrier layer region exposed to the surface, the strong polarization field in this region may move the photogenerated holes towards the surface and neutralize the trapped surface electrons, resulting in a positive virtual gate bias and a consequent increase of the channel photocurrent. However, in the PG-HFEPT, the contribution from this part can be considered negligible. From the peak absorption coefficient at the absorption edge [21] and the proportion in the total effective detection area, it can be estimated that only less than 10% of the absorbable incident DUV light is absorbed in the 25 nm thick $Al_{0.6}GaN$ barrier layer outside the p^+-photogate. This is also supported by the results shown in Fig. 3(d), which does not show an obvious increase in the I_{ph} or responsivity at ~250 nm corresponding to the absorption edge of $Al_{0.6}GaN$. For incident DUV light with a wavelength greater than 250 nm, however, it is basically not absorbed in the $Al_{0.6}GaN$ barrier layer. Therefore, the I_{ph} is dominantly induced by the top and back photogating effects.

Based on the above factors, the total change of the channel photocurrent can be regarded as the sum of the photocurrent increased under the action of the top p-type photogate and the virtual back photogate, i.e.,

$$I_{ph} = I_{pht} + I_{phb} = V_{pht} \cdot g_{mt} + V_{phb} \cdot g_{mb}, \quad (1)$$

where I_{pht} and I_{phb} are the channel photocurrent induced by the photovoltage in the top p-type photogate (V_{pht}) and the virtual back photogate (V_{phb}) [22], respectively, and g_{mt} and g_{mb} are the transconductance due to the top and back photogate, respectively. The photovoltage V_{ph} (V_{pht} or V_{phb}) is similar to the open-circuit voltage of p-n junction solar cells, which is given by [23]

$$V_{ph} = \frac{nkT}{q} \ln\left(\frac{I_{pph}}{I_{rs}} + 1\right), \quad (2)$$

where k is the Boltzmann's constant, T is the temperature, I_{pph} is the primary photocurrent generated in the p-i-n heterojunction of the top photogate (I_{ppht}) or generated in the channel layer of the back photogate (I_{pphb}), and I_{rs} is the reverse saturation current. The transconductance g_m (g_{mt} or g_{mb}) can be given by [24]

$$g_m = A_g C_g / t_e, \quad (3)$$

where A_g is the total area of the top p^+-$Al_{0.4}GaN$ photogate (A_{tg}) or the back photogate (A_{bg}), C_g is the capacitance per unit area between the 2DEG channel and the top gate (C_{tg}) or between the 2DEG channel and the back gate (C_{bg}), and t_e is the transit time of the channel electrons under the gate. The capacitance of top or back photogate, however, can be estimated from the semiconductor dielectric constant ε_s and the depletion region width (W_g) of the gate, i.e., $C_g = \varepsilon_s / W_g$. The transit time t_e is defined as the time when the electrons in the conductive channel move between the electrodes, which can be given by $t_e = L/\mu_n E$, where L is the distance between electrodes, μ_n is the mobility of electrons in the conductive channel (2DEG channel), and E is the electric field.

Using the above equations, the theoretical I_{ph} and optical gain of the PG-HFEPT under 5 V bias are calculated to be 7.7×10^{-4} A and 1.8×10^5, respectively. In the calculation of photovoltage V_{ph}, the primary photocurrent I_{pph} was obtained from $qP_{in}/h\nu$, in which the P_{in} was estimated by considering the light receiving area, thickness, and absorption coefficient of each epilayer in the active region and the reflectivity of the PG-HFEPT wafer surface at 260 nm. Moreover, the absorption coefficients of uid- and p^+- $Al_{0.4}GaN$ epilayers were calculated from the transmission spectra of their respective thin film samples (not shown in this paper). The value of I_{rs} was obtained by extrapolating the linear region of the dark I-V curve of the photogate junction to zero applied voltage. An ideality factor of 1.5 was supposed for the top photogate heterojunction, and a value of 1.0 was used for the back-photogate junction. In the estimation of transconductance g_m, the widths of the absorber layer and the channel layer were taken as the W_g values of the top and back photogates. As expected, the theoretical optical gain matches well with the experimental gain value of 7.5×10^4. The calculated gain values under other bias voltages are also in good agreement with the measured values, confirming that the gain mechanism in the PG-HFEPT is the current amplification due to the dual photogating effect, in which the gate voltages are modulated by incident DUV light.

To further assess the performance of the PG-HFEPT, we investigate the incident power dependency of the photoresponse. Figure 5(a) gives the I_{ph}-V curves measured under the 260 nm LED illumination with different power densities. One

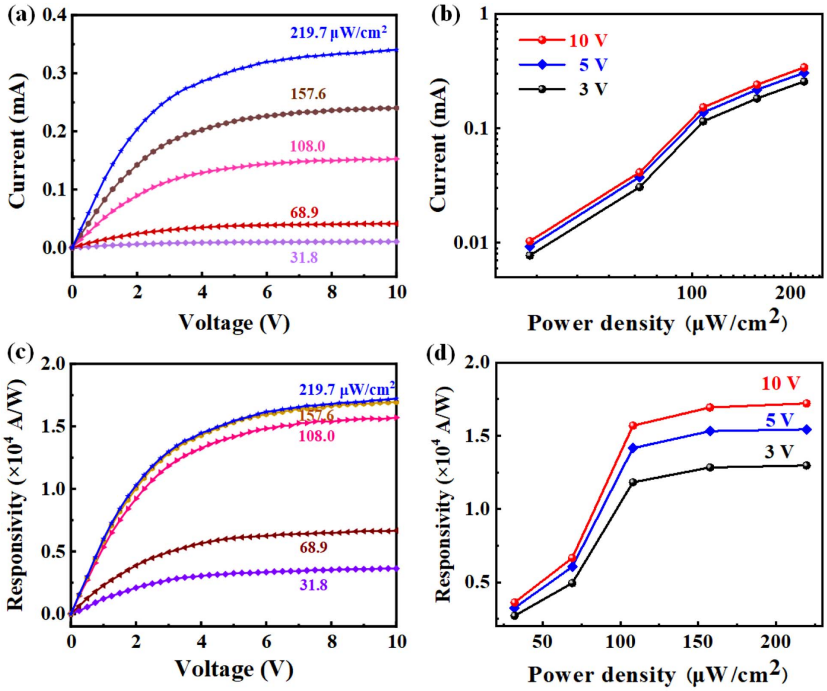

Fig. 5. (a) I_{ph}-V curves of the PG-HFEPT measured at different incident power densities of a 260 nm LED. (b) Dependence of I_{ph} on incident power density. (c) Responsivity versus voltage characteristics under different incident power densities. (d) Dependence of responsivity on incident power density.

can see that the I_{ph} is regulated by both the incident light power density and the bias voltage. The I_{ph} shows a weak linear dependence on the incident power density at a lower power density and shows a linear dependence as the power density increases to 100 $\mu\mathrm{W/cm^2}$ [Fig. 5(b)]. Under different incident power densities, the responsivity increases with the increase of bias voltage in the range of 0 to 10 V as shown in Fig. 5(c). This enhancement in responsivity is attributed to the shortening of the channel electron transition time (t_e) under the increased bias, which increases the transconductance and the corresponding channel photocurrent. It can also be seen that the responsivity increases with the incident power density [Fig. 5(d)]. When the power density reaches 100 $\mu\mathrm{W/cm^2}$, however, the responsivity tends to be constant, indicating that the photocurrent increases linearly with the incident light power, that is, the photovoltages in the top and back photogates have reached the maximum.

One of the most important specifications of photodetector is the detectivity. Normalized signal-to-noise performance of a photodetector is usually described by specific detectivity D^*. Generally, three types of noise can be found in the semiconductor photodetector, namely, shot noise, Johnson noise (or thermal noise), and flicker ($1/f$) noise. The shot noise is related to the statistical fluctuation in the current flow, which is characterized by a noise current power density of $\langle I_S^2 \rangle = 2qI$, where I is the total current including I_{dark} and I_{ph} flowing through the detector. Another type of noise, Johnson noise, is generated by the thermal motion of the electrons. Its current power density is represented by $\langle I_J^2 \rangle = 4kT/R_d$, where R_d is the dynamic resistance (differential resistance) of detector at a given bias. Moreover, flicker noise with a spectral power density proportional to $1/f$ is usually observed at low frequency while measuring shot and Johnson noise.

If the shot noise from the dark current is the dominant contribution, the specific detectivity can be calculated by $D_S^* = R_\lambda \sqrt{A/(2qI_{\mathrm{dark}})}$, where R_λ is the responsivity at a specific wavelength and A is the effective detection area. For the PG-HFEPT, we obtained $I_{\mathrm{dark}} = 7.80 \times 10^{-13}$ A and $D_{\mathrm{TS}}^* = 2.92 \times 10^{17}$ cm $\mathrm{Hz^{1/2}\,W^{-1}}$ at 260 nm and 5 V bias. Furthermore, the Johnson noise and shot noise limited D^* can be calculated using the equation [25]

$$D_{\mathrm{TS}}^* = \frac{R_\lambda \sqrt{A}}{\sqrt{2qI_{\mathrm{dark}} + 4kT/R_d}}. \tag{4}$$

The detectivity D_{TS}^* was then calculated to be 2.91×10^{17} cm $\mathrm{Hz^{1/2}\,W^{-1}}$ at 260 nm.

A more accurate evaluation of detectivity, however, is to take into account the flicker noise at low frequency. Accordingly, the noise power spectra were measured from the two HFEPTs in the frequency range of 1 Hz to 100 kHz at bias voltages of 1 and 5 V as shown in Fig. 6(a). Compared with the HFEPT, the noise power density of the PG-HFEPT is more than 3 orders of magnitude lower, and the dispersion of the spectral density is smaller under different bias voltages. The measured noise power spectrum is described by $S_N(f) = K(S_1/f^\gamma)$, where S_N is the spectral density of the noise power, K is a constant, S_1 is the noise power at 1 Hz, f is the frequency, and γ is the fitting parameter. From the measured spectra, the γ values are found to be almost unity throughout the measured frequency range, indicating that the low-frequency noise in our devices was dominated by $1/f$ (flicker) type noise. The total noise current power can be evaluated by integrating the noise power

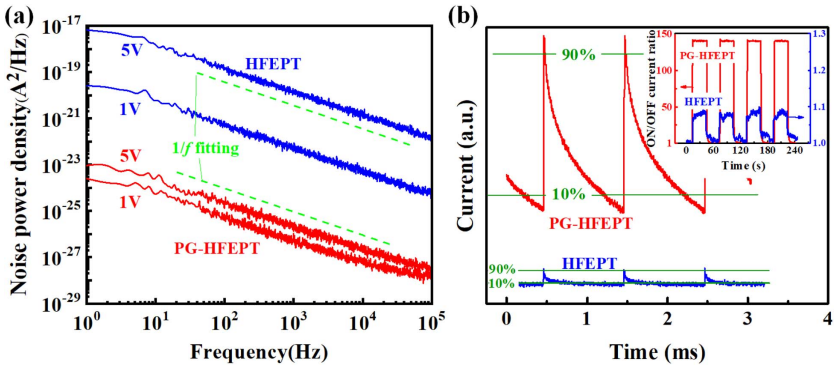

Fig. 6. (a) Noise power density spectra of the PG-HFEPT and HFEPT measured at different biases. (b) Impulse response of the two phototransistors measured at 3 V bias. The inset is the time-dependent photoresponse of the two phototransistors at 3 V bias measured at 260 nm irradiation with a 30 s on/off cycle.

density $S_N(f)$ over the frequency range $\langle I_N^2 \rangle = \int S_N(f)\mathrm{d}f$. Therefore, the noise equivalent power (NEP) can be determined by $\mathrm{NEP} = \sqrt{\langle I_N^2 \rangle}/R_\lambda$, while the specific detectivity D^* considering the flicker noise can then be calculated by

$$D^* = \sqrt{A}\sqrt{\mathrm{BW}}/\mathrm{NEP}, \tag{5}$$

where BW is the measured bandwidth. For a given bandwidth of 100 kHz and a bias voltage of 5 V, the NEP of our HFEPT was obtained as 8.38×10^{-13} W. The corresponding D^* value is 3.61×10^{12} cm Hz$^{1/2}$ W^{-1}. In comparison, the NEP of the PG-HFEPT was estimated to be 1.07×10^{-15} W, which leads to an ultrahigh D^* of 2.84×10^{15} cm Hz$^{1/2}$ W^{-1}. We believe that the suppression of dark current by the p$^+$-AlGaN photogate is a main factor for the reduction of NEP and the enhancement of detectivity.

The transient responses of the phototransistors were also characterized. In the measurements, the pulse width of the 260 nm light was 625 ps, and the repetition rate was 1 kHz. Figure 6(b) gives the impulse responses measured at a bias of 3 V. The rise (τ_r) and fall (τ_f) times, defined as the time interval of the current rising from 10% to 90% and dropping from 90% to 10% of the peak value, are 4.4 and 591 μs, respectively, for the PG-HFEPT. These response speeds are much faster than that of the most solar-blind UV photodetectors reported [26–29]. Although the impulse response amplitude of the HFEPT is much lower than that of the PG-HFEPT due to the large dark current, the τ_r and τ_f (1.4 and 250 μs) of its impulse response are quite faster than those of PG-HFEPT. Since the electron transition time t_e is estimated to be ~3.7 ns, the rise time is thus likely limited by the RC constant. This assumption is also consistent with the longer τ_r of the PG-HFEPT showing higher Ohmic contact resistance.

The much longer τ_f compared with the τ_r in both phototransistors is speculated to associate with the persistent photoconductivity (PPC) effect caused by the trapping/detrapping process of photogenerated carriers at deep level defects, which is commonly observed in the AlGaN/GaN-based HFETs [30,31]. For the slower response decay in the PG-HFEPT, one possible reason is that the ICP etching introduces the increment of deep-level defects in the active region, especially in the barrier layer, which exacerbates the PPC effect.

Shown in the inset of Fig. 6(b) are the time-dependent photoresponses of the two phototransistors at 3 V bias measured by periodically turning on and off the 260 nm incident light. The responses are given in the form of on/off current ratio to more clearly show the difference between the responses of the two devices. Both phototransistors showed good stability and reproducibility to the periodic 260 nm irradiation. Benefiting from

Table 1. Comparison of Characteristic Parameters of Our Detectors Using Dual-Photogating Effects to Those of Published Solar-Blind UV Photodetectors

Material	Type	D^* (cm Hz$^{1/2}$ W^{-1})	R (A/W)	I_{ph}/I_{dark} ratio	τ_r/τ_f (ms)	Refs.
AlGaN	HFEPT	2.84×10^{15} 2.91×10^{17} [a]	1.9×10^4 (5 V)	1.0×10^8	0.0044/0.591	This work
$Cu_2O/\beta\text{-}Ga_2O_3$	Heterojunction	5.20×10^{11} [b]	0.053 (−16 V)	—	200/200	[26]
$Cs_3Cu_2I_5/\beta\text{-}Ga_2O_3$	Heterojunction	2.40×10^8	0.0023 (0 V)	5.1×10^4	37/45	[27]
$\beta\text{-}Ga_2O_3$	MSM	9.8×10^{15} [b]	46 (20 V)	1.0×10^8	0.0009/0.0119	[28]
AlGaN	MSM	1.76×10^{12} [b]	3.63 (5 V)	—	1130/133	[29]
AlGaN	p-i-n	4.20×10^{14} [c]	0.131 (5 V)	4.8×10^5	140/8200	[32]
AlGaN/GaN	Schottky	2.60×10^{12} [c]	0.09 (50 V)	—	—	[33]
AlGaN	p-i-n	2.00×10^{14} [c]	0.09 (5 V)	—	—	[34]
AlGaN	APD	1.40×10^{14} [c]	0.13 (20 V)	1.0×10^3	—	[35]

[a]Johnson and shot noise limited D^*.
[b]Shot noise limited D^*.
[c]Johnson noise limited D^*.

the low dark current, the PG-HFEPTs demonstrate an on/off current ratio of 2 orders of magnitude higher than HFEPT.

To better understand the performance level of our device, Table 1 compares the main characteristic parameters of our PG-HFEPT with those of the representative solar blind UV photodetectors reported previously. It is shown that the solar-blind PG-HFEPTs have a record high specific detectivity. Moreover, the I_{ph}/I_{dark} ratio and response speed are also superior to most reported solar-blind UV detectors. The excellent performance suggests that the two-terminal PG-HFEPT using the dual-photogating effect is a promising candidate for highly sensitive solar-blind UV detection.

4. CONCLUSIONS

In conclusion, solar-blind AlGaN HFEPTs utilizing dual-float-photogating effect have been reported. The fabricated devices with an interdigital configuration exhibit a very low dark current of less than 2 pA in the bias range of 0 to 10 V, due to the effective depletion of the 2DEG channel by the p^+-AlGaN top photogate. High optical gain of 7.5×10^4 and photo-to-dark current ratio of 4.0×10^8 were also demonstrated under 5 V bias. This high optical gain (photocurrent) is attributed to the dual-photogating effect under the joint action of the top p^+-$Al_{0.4}GaN$ gate and polarization-induced virtual back gate. Based on the above factors, a record high specific detectivity of 2.84×10^{15} cm $Hz^{0.5}$ W^{-1} was realized in the phototransistors. Moreover, the phototransistors show a quite high response speed with a rise time of 4.4 μs and a fall time of 591 μs. Device performance is believed to be further improved by enhancing the 2DEG mobility. The two-terminal HFEPT using the dual-float-photogating effect is, therefore, a very competitive option for integrated and high-sensitivity solar-blind UV detection.

Funding. National Key Research and Developtment Program of China (2016YFB0400901); State Key Program of National Natural Science Foundation of China (61634002); Key Realm RD Program of Guangdong Province (2019B010132004, 2020B010172001); Key Realm RD Program of Guangzhou (202103030002).

Disclosures. The authors declare no conflicts of interest.

Data Availability. Data underlying the results presented in this paper are not publicly available at this time but may be obtained from the authors upon reasonable request.

†These authors contributed equally to this paper.

REFERENCES

1. C. Xie, X. T. Lu, X. W. Tong, Z. X. Zhang, F. X. Liang, L. Liang, L. B. Luo, and Y. C. Wu, "Recent progress in solar-blind deep-ultraviolet photodetectors based on inorganic ultrawide bandgap semiconductors," Adv. Funct. Mater. **29**, 1806006 (2019).
2. M. Razeghi, "Short-wavelength solar-blind detectors: status, prospects, and markets," Proc. IEEE **90**, 1006–1014 (2002).
3. G. Chen, F. Abou-Galala, Z. Xu, and B. M. Sadler, "Experimental evaluation of LED-based solar blind NLOS communication links," Opt. Express **16**, 15059–15068 (2008).
4. Y. F. Wu, D. Kapolnek, J. P. Ibbetson, P. Parikh, B. P. Keller, and U. K. Mishra, "Very-high power density AlGaN/GaN HEMTs," IEEE Trans. Electron Devices **48**, 2181–2183 (2001).
5. T.-M. Kuan, S.-J. Chang, Y.-K. Su, C.-H. Ko, J. B. Webb, J. A. Bardwell, Y. Liu, H. Tang, W.-P. Lin, Y.-T. Cherng, and W.-H. Lan, "High optical-gain AlGaN/GaN_2 dimensional electron gas photodetectors," Jpn. J. Appl. Phys. **42**, 5563–5564 (2003).
6. A. Yoshikawa, S. Ushida, K. Nagase, M. Iwaya, T. Takeuchi, S. Kamiyama, and I. Akasaki, "High-performance solar-blind $Al_{0.6}Ga_{0.4}N/Al_{0.5}Ga_{0.5}N$ MSM type photodetector," Appl. Phys. Lett. **111**, 191103 (2017).
7. H. L. Wu, W. C. Wu, H. X. Zhang, Y. D. Chen, Z. S. Wu, G. Wang, and H. Jiang, "All AlGaN epitaxial structure solar-blind avalanche photodiodes with high efficiency and high gain," Appl. Phys. Express **9**, 052103 (2016).
8. Z. G. Shao, D. J. Chen, H. Lu, R. Zhang, D. P. Cao, W. J. Luo, Y. D. Zheng, L. Li, and Z. H. Li, "High-gain AlGaN solar-blind avalanche photodiodes," IEEE Electron Device Lett. **35**, 372–374 (2014).
9. L. X. Zhang, S. J. Tang, C. S. Liu, B. Li, H. L. Wu, H. L. Wang, Z. S. Wu, and H. Jiang, "Demonstration of solar-blind $Al_xGa_{1-x}N$-based heterojunction phototransistors," Appl. Phys. Lett. **107**, 233501 (2015).
10. L. J. Sun, Z. S. Lv, Z. H. Zhang, X. J. Qiu, and H. Jiang, "High-performance AlGaN heterojunction phototransistor with dopant-free polarization-doped p-base," IEEE Electron Device Lett. **41**, 325–328 (2020).
11. T. Narita, A. Wakejima, and T. Egawa, "Ultraviolet photodetectors using transparent gate AlGaN/GaN high electron mobility transistor on silicon substrate," Jpn. J. Appl. Phys. **52**, 01AG06 (2013).
12. A. M. Armstrong, B. Klein, A. A. Allerman, E. A. Douglas, A. G. Baca, M. H. Crawford, G. W. Pickrell, and C. A. Sanchez, "Visible-blind and solar-blind detection induced by defects in AlGaN high electron mobility transistors," J. Appl. Phys. **123**, 114502 (2018).
13. Q. F. Lyu, H. X. Jiang, and K. M. Lau, "High gain and high ultraviolet/visible rejection ratio photodetectors using p-GaN/AlGaN/GaN heterostructures grown on Si," Appl. Phys. Lett. **117**, 071101 (2020).
14. M. Iwaya, S. Miura, T. Fujii, S. Kamiyama, H. Amano, and I. Akasaki, "High-performance UV detector based on AlGaN/GaN junction heterostructure-field-effect transistor with a p-GaN gate," Phys. Status Solidi C **6**, S972–S975 (2009).
15. M. A. Khan, Q. Chen, J. N. Kuznia, C. J. Sun, and M. S. Shur, "Gated photodetector based on GaN/AlGaN heterostructure field effect transistor," Electron. Lett. **31**, 398–400 (1995).
16. S. H. Baek, G. W. Lee, C. Y. Cho, and S. N. Lee, "Gate-controlled amplifiable ultraviolet AlGaN/GaN high-electron-mobility phototransistor," Sci. Rep. **11**, 7172 (2021).
17. X. J. Qiu and H. Jiang, "Highly conductive and 260 nm transparent p-type $Al_{0.6}Ga_{0.4}N$ achieved utilizing interface doping effects," Cryst. Growth Des. **21**, 2389–2397 (2021).
18. H. Jiang, G. Y. Zhao, H. Ishikawa, T. Egawa, T. Jimbo, and M. Umeno, "Determination of exciton transition energy and bowing parameter of AlGaN alloys in AlGaN/GaN heterostructure by means of reflectance measurement," J. Appl. Phys. **89**, 1046–1052 (2001).
19. P. Cantu, F. Wu, P. Waltereit, S. Keller, A. E. Romanov, S. P. DenBaars, and J. S. Speck, "Role of inclined threading dislocations in stress relaxation in mismatched layers," J. Appl. Phys. **97**, 103534 (2005).
20. A. Jiménez, Z. Bougrioua, J. M. Tirado, A. F. Braña, E. Calleja, E. Muñoz, and I. Moerman, "Improved AlGaN/GaN high electron mobility transistor using AlN interlayers," Appl. Phys. Lett. **82**, 4827–4829 (2003).
21. K. Takeuchi, S. Adachi, and K. Ohtsuka, "Optical properties of $Al_xGa_{1-x}N$ alloy," J. Appl. Phys. **107**, 023306 (2010).
22. Z. H. Zaidi and P. A. Houston, "Highly sensitive UV detection mechanism in AlGaN/GaN HEMTs," IEEE Trans. Electron Devices **60**, 2776–2781 (2013).
23. M. A. Green, "Solar cells—operating principles, technology and system applications," Sol. Energy **28**, 447 (1982).
24. S. M. Sze and K. K. Ng, *Physics of Semiconductor Devices*, 3rd ed. (Wiley, 2006).

25. B. Chen, W. Y. Jiang, J. Yuan, A. L. Holmes, and B. M. Onat, "Demonstration of a room-temperature InP-based photodetector operating beyond 3 μm," IEEE Photon. Technol. Lett. **23**, 218–220 (2011).
26. H. Bae, A. Charnas, X. Sun, J. Noh, M. Si, W. Chung, G. Qiu, X. Lyu, S. Alghamdi, H. Wang, D. Zemlyanov, and P. D. Ye, "Solar-blind UV photodetector based on atomic layer-deposited Cu_2O and nanomembrane β-Ga_2O_3 pn oxide heterojunction," ACS Omega **4**, 20756–20761 (2019).
27. J. Ma, X. Xia, S. Yan, Y. Li, W. Liang, J. Yan, X. Chen, D. Wu, X. Li, and Z. Shi, "Stable and self-powered solar-blind ultraviolet photodetectors based on a $Cs_3Cu_2I_5$/β-Ga_2O_3 heterojunction prepared by dual-source vapor codeposition," ACS Appl. Mater. Interfaces **13**, 15409–15419 (2021).
28. B. S. Qiao, Z. Z. Zhang, X. H. Xie, B. H. Li, K. X. Li, X. Chen, H. F. Zhao, K. W. Liu, L. Liu, and D. Z. Shen, "Avalanche gain in metal-semiconductor-metal Ga_2O_3 solar-blind photodiodes," J. Phys. Chem. C **123**, 18516–18520 (2019).
29. S. C. Wu, M. J. Wu, and Y. F. Chen, "Nanolayered graphene/hexagonal boron nitride/n-AlGaN heterostructures as solar-blind deep-ultraviolet photodetectors," ACS Appl. Nano Mater. **3**, 7595–7603 (2020).
30. J. Z. Li, J. Y. Lin, H. X. Jiang, M. A. Khan, and Q. Chen, "Persistent photoconductivity in a two-dimensional electron gas system formed by an AlGaN/GaN heterostructure," J. Appl. Phys. **82**, 1227–1230 (1997).
31. J. Sun, T. Zhan, Z. Liu, J. Wang, X. Yi, P. M. Sarro, and G. Zhang, "Suppression of persistent photoconductivity AlGaN/GaN heterostructure photodetectors using pulsed heating," Appl. Phys. Express **12**, 122007 (2019).
32. A. Kalra, S. Rathkanthiwar, R. Muralidharan, S. Raghavan, and D. N. Nath, "Material-to-device performance correlation for AlGaN-based solar-blind p-i-n photodiodes," Semicond. Sci. Technol. **35**, 035001 (2020).
33. N. Biyikli, O. Aytur, I. Kimukin, T. Tut, and E. Ozbay, "Solar-blind AlGaN-based Schottky photodiodes with low noise and high detectivity," Appl. Phys. Lett. **81**, 3272–3274 (2002).
34. C. J. Collins, U. Chowdhury, M. M. Wong, B. Yang, A. L. Beck, R. D. Dupuis, and J. C. Campbell, "Improved solar-blind detectivity using an $Al_xGa_{1-x}N$ heterojunction p-i-n photodiode," Appl. Phys. Lett. **80**, 3754–3756 (2002).
35. T. Tut, M. Gokkavas, A. Inal, and E. Ozbay, "$Al_xGa_{1-x}N$-based avalanche photodiodes with high reproducible avalanche gain," Appl. Phys. Lett. **90**, 163506 (2007).